

Supporting Information For: Tunable Cu-Enrichment Enables Designer Syngas Electrosynthesis from CO₂

Michael B. Ross,^{1,2} Cao Thang Dinh,^{2,3} Yifan Li,^{1,4} Dohyung Kim,⁵ Phil De Luna,^{2,6} Edward H. Sargent^{*2,3}, Peidong Yang,^{*1,2,4,5,7,8}

¹Department of Chemistry, University of California, Berkeley, Berkeley, CA 94720, USA

²Bio-inspired Solar Energy Program, Canadian Institute for Advanced Research, Toronto, Ontario M5G 1Z8, Canada.

³Department of Electrical and Computer Engineering, University of Toronto, Toronto, Ontario, M5S 3G4, Canada.

⁴Chemical Sciences Division, Lawrence Berkeley National Laboratory, Berkeley, CA 94720, USA

⁵Department of Materials Science and Engineering, University of California, Berkeley, Berkeley, CA 94720, USA

⁶Department of Materials Science and Engineering, University of Toronto, Toronto, Ontario, M5S 3E4, Canada.

⁷Materials Sciences Division, Lawrence Berkeley National Laboratory, Berkeley, CA 94720, USA

⁸Kavli Energy Nanosciences Institute, University of California, Berkeley, Berkeley, CA 94720, USA

Materials and Methods:

Preparation of SERS-Active Electrodes

Au electrodes were roughened in 0.1 M KCl (Sigma) using a procedure described previously for generating SERS-active substrates.¹ First, gold foil (Sigma, 99.99% trace metals basis) was cleaned electrochemically in 0.1 M H₂SO₄ (Sigma, 99.999%) using five cyclic voltammetry cycles from 0.2-1.50 V vs. 1 M Ag/AgCl at a scan rate of 50 mV/s. The foil was then rinsed with Nanopure water, immersed in a 0.1 M KCl solution, and subjected to 25 oxidation-reduction cycles from -0.28 (5 s hold) to -1.22 (10 s hold) V vs. Ag/AgCl at 500 mV/s to render the substrate SERS-active. After thorough rinsing with Nanopure water, underpotential deposition of Cu was performed by immersing the substrate in 1 mM CuSO₄ (Sigma, 99.99% trace metals basis), 0.5 M H₂SO₄ solution. Cyclic voltammetry was performed to characterize the Cu underpotential

deposition region (approximately 0.08-0.48 vs. Ag/AgCl), and oxidation-reduction sweeps at 50 mV/s were performed across the region of interest, ending with a cathodic wave, until the voltammograms were stable (minimum of 5 waves). To increase the Cu coverage, increasing fractions of the CV windows were included in the sweeps (1/3, 2/3 and 3/3, as described in the main text). For Cu SERS, Cu foil (Alfa Aesar, 99.999% trace) was roughened in a similar procedure as described above for gold; for Cu a 1.0 M KCl solution was used and the potentials for oxidation-reduction were -0.4 (10 s hold) to -1.0 (1 s hold) for 15 cycles at 100 mV/s.

Scanning electron microscopy

Scanning electron microscopy (SEM) was performed using a JEOL SEM JSM-6340F at 12 μ A and 5 keV. Samples were rinsed with Nanopure water prior to imaging and were then mounted with double-sided Cu tape (Ted Pella).

X-ray photoemission spectroscopy

X-ray photoemission spectroscopy (XPS) was performed using a PHI-5400 XPS. Measurements were performed at $\sim 4 \times 10^{-9}$ Torr with an Al K α source and a pass energy of 17.9 eV. For analysis, the spectra were corrected using a Shirley background and the relative compositions were determined using the appropriate atomic sensitivity factors for Au 4f and Cu 2p, respectively.

Electrochemical surface-enhanced Raman spectroscopy

SERS was performed using a Jobin-Yvon LabRAM HR confocal microscope with 20X (0.25 N.A) objective and a custom-made Teflon electrochemical cell. A 633 nm laser (10-40 mW) was focused on the roughened metal electrode and the Raman scattered photons were dispersed by a 1800 g/cm grating and collected by a spectrometer. Typical collections times ranged from 10-30s. For analysis, SER spectra were normalized by laser power and collection time and corrected by a linear baseline.

In situ spectroelectrochemistry was performed using a Gamry Interface 1000 potentiostat, a Pt counter electrode (Alfa Aesar, Pt gauze 52 mesh woven from 0.1 mm diameter wire, 99.9% trace metals basis), and a Ag/AgCl 1 M KCl reference electrode (CH Instruments) in ~ 30 mL of 0.1 M KHCO₃. The electrolyte was synthesized using K₂CO₃ (Sigma, anhydrous 99.99% trace metals basis) that was bubbled overnight with CO₂, and subsequently pre-electrolyzed at 10 μA for ~12 hours to remove trace metal impurities. During a measurement, CO₂ (Praxair, 5.0 Ultra high purity) was bubbled at ~ 20 mL min⁻¹; prior to each measurement CO₂ was bubbled for 10 min to ensure saturation. Typically, SERS measurements were performed using chronoamperometry set at the potential of interest to ensure steady state conditions.

Theoretical Calculations

Electronic, vibrational, and thermodynamic quantities were calculated using density functional theory (DFT) with the generalized gradient approximation (GGA) Perdew-Becke-Ernzerh (PBE) exchange-correlation functional² in a projector augmented

wave (PAW) implementation using the Vienna *ab initio* Simulation Package (VASP).³ The PBE functional has been shown to provide reasonable agreement with experiment for CO and other CO₂-derived molecules on noble metal surfaces.⁴⁻⁵ The PAW pseudopotentials⁶⁻⁷ were used to calculate interactions with a cutoff energy of 500 eV, a (5x5x1) Monkhorst-Pack mesh,⁸ Fermi-level smearing of 0.1 eV, spin polarization, and a dipole correction.⁹ Slab geometries were all 3x3x3 slabs of (111) surfaces with 15 Å of vacuum. The surface slabs were relaxed using the Broyden–Fletcher–Goldfarb–Shannon (BFGS) algorithm¹⁰ until the maximum force was less than 0.2 eV/atom. Subsequent optimization, thermodynamic, vibrational, and electronic calculations were performed beginning with the optimized slabs where the bottom two layers were fixed. In all cases, CO is adsorbed in the ontop position and H is adsorbed in hollow fcc sites.

Thermodynamic and vibrational calculations were performed using the open-source atomic simulation environment (ASE) package.¹¹ Gibbs free energies were calculated at 298 K and 1 atmosphere according to

$$G = H - TS = E_{\text{Electronic}} + E_{\text{ZPV}} + \int_0^{298} C_v dT - TS$$

where $E_{\text{Electronic}}$ is the DFT-optimized total energy, E_{ZPE} is the zero-point vibrational energy, $C_v dT$ is the heat capacity, T is the temperature, and S is the entropy. Gas-phase CO₂ and H₂ were treated using the ideal gas approximation and adsorbates were treated using the harmonic oscillator approximation for all degrees of freedom. The calculated energies for CO₂ and H₂ were corrected by -0.51 and -0.08 eV, respectively, to account for imperfect estimation by DFT.⁴ Binding energies were calculated by

$$E_{\text{Ads}} = E_{\text{Adsorbate}^*} (E_{\text{Slab}} - E_{\text{Gas}})$$

where E_{Ads} is the adsorption energy (ΔG_{Ads}), $E_{\text{Adsorbate}^*}$ is the energy of the adsorbate-slab geometry, E_{Surf} is the energy of the bare slab, and E_{Gas} is the energy of the molecule in the gas phase. For comparison with experimental SER spectra, the vibrational frequencies were broadened and fit by a Lorentzian distribution with a full-width half maximum of 10 cm^{-1} . Bader partial atomic charges were determined using the DFT calculated electron density as input into the Bader Charge Analysis module.¹²

Au Needle Electrocatalyst Synthesis

Au nanoneedles and Cu UPD-modified nanoneedles were synthesized by electrodeposition from a HAuCl_4 (Sigma, 99.999% trace metals basis) and HCl solution.⁵ In particular, a 1 cm^2 area of carbon paper (Fuel-cell store) was immersed into a 160 mM HAuCl_4 , 0.5 M HCl solution and chronoamperometry was performed at -0.4 V vs. Ag/AgCl (in 3M KCl) for 300 s. Cu UPD was performed as described above without modification.

Electrochemical Testing

All electrocatalytic testing was performed using a three-electrode system connected to an electrochemical workstation (Autolab PGSTAT302N) where Ag/AgCl (with 3M KCl as the filling solution) and platinum mesh were used as reference and counter electrodes, respectively. Testing was performed in CO_2 -saturated 0.5 M KHCO_3 electrolyte in a gas-tight two-compartment H-cell separated by an ion exchange membrane (Nafion117). The KHCO_3 electrolyte was bubbled with CO_2 for 1 hour before each measurement. The electrolyte was stirred at a constant 300 r.p.m. during electrolysis

with CO₂ gas being delivered into the cathodic compartment at a rate of 20.00 standard cubic centimeters per minute (s.c.c.m.). Product were directed into a gas chromatograph (PerkinElmer Clarus 600) equipped with a Molecular Sieve 5A capillary column, a packed Carboxen-1000 column, and argon (Linde, 99.999%) was used as the carrier gas. The columns led directly to a thermal conductivity detector to quantify hydrogen and a flame ionization detector equipped with a methanizer to quantify carbon monoxide. The partial current densities of CO and H₂ production were calculated as reported previously.⁵ All Faradaic efficiencies were >95% CO and H₂; liquid analysis by nuclear magnetic resonance (NMR) spectroscopy typically showed the presence of trace electrosynthesized formate.

Supporting Discussion 1: Commentary on CO* site variation in SERS

While it is likely that a variety of coordination sites are accessible in the *in situ* SERS experiment, the observed $\nu_{\text{C-O}}$ exhibit a single peak with similar linewidths for all Cu-enriched substrates. This behavior is indicative of a single dominant adsorbed species, rather than a superposition of two different CO* coordination environments being averaged in the experiment. In other words, if CO* were present at two chemically distinct sites in similar amounts, one would expect to observe multiple and/or broadened peaks (similar to what is observed on bulk Cu, **Figure 3c**, red). From these data, one cannot discern which site CO* is at due to the complex influence of kinetics and competition with HER. It is worth noting that the magnitude of SERS enhancement varies across the substrate, though this variation was mostly apparent on the bare Au (where some sites gave very little signal in comparison with those included here), consistent with prior reports.¹³⁻¹⁴

Supporting Discussion 2: Non-Linear Relationships between $\nu_{\text{C-O}}$, $d_{\text{C-O}}$, $d_{\text{M-C}}$, and ΔG_{Ads}

Typically, it is assumed that the C-O bond length ($d_{\text{C-O}}$), which is inversely related to the vibrational frequency $\nu_{\text{C-O}}$ (**Figure S8a**), is also inversely and linearly related to the metal-CO bond length ($d_{\text{M-C}}$) as well as the adsorbate binding energy.¹⁵ This assumption is inferred through the Badger's rule, which is based upon the Blyholder model, the seminal model by which metal-CO binding can be understood.¹⁶⁻¹⁸ As described in the main text, metal-CO bonding involves 5σ donation from CO into the d-band of the metal, which then leads to a proportional amount of electron density being

donated back to the $2\pi^*$ orbitals in CO. Within this description, a greater extent of 5σ donation results in a shorter M-CO bond (due to a stronger bonding interaction) and longer C-O bond (due to the backdonation into $2\pi^*$). While this model describes the dominant trends on the periodic table for transition metal bonding with CO,¹⁷ in addition to the site dependence of bonding for ontop, bridge, and hollow sites,¹⁵ there are systems where the interaction between CO and a complex metal surface are not fully described. For example, the 4σ and 1π orbitals can contribute to interactions that are far more complex,^{15, 19} whereby these systems involve a complex balance of repulsive and attractive interactions.²⁰⁻²¹ Additionally, similar non-intuitive relationships between CO binding and vibrational character have been observed in Pt-Ru mixed metallic systems.²² Note that in this work, the Blyholder model does qualitatively explain the red-shifts that are observed with increasing Cu enrichment for CO* (**Figure 3**).

However, in the Cu-enriched Au slabs studied here, it is clear that there is not a linear relationship between the C-O and M-CO bond lengths (**Figure S8**). Indeed, it is seen in **Figures S9-10** that site adsorption preference and extent of Cu-enrichment can change both the relative energies (from the Fermi level E_f) and filling extent of the orbitals involved in bonding, which can complicate the repulsive and attractive interactions that occur at the M-CO interface. Finally, the more simplistic Bader charge analysis (**Figure S11**), which describes the partial electronic charge associated with each atom, suggests that the nearest-neighbor interactions indeed are important for understanding the thermodynamics of CO* bonding (**Figure 3**). Interestingly, the Bader charge at the adsorption site increases linearly for CO* at either Cu or Au sites. For the nearest neighbor atoms around Au sites, the Bader charges decrease linearly with

increasing Cu content; additionally d_{C-O} , d_{M-C} , v_{C-O} , and ΔG_{Ads} all vary linearly as well. However, for CO^* at Cu sites, d_{C-O} and v_{C-O} linearly vary (**Figure S8a**); but there is not a discernible relationship between those quantities and the Bader nearest-neighbor charge, d_{M-C} , and ΔG_{Ads} . As noted in the main text, for CO^* at Cu sites the nearest-neighbor Bader charge exhibits a similar non-monotonic trend to both d_{M-C} and ΔG_{Ads} . Thus, both Au and Cu sites present distinct chemical environments as well as extents of nearest-neighbor atom interactions with CO^* .

It should be noted that none of these quantities produce a clear discernible means by which these descriptors can be understood; for example bulk Au and Cu have similar Bader charge quantities at the adsorption site, despite the pronounced differences between Au and Cu in v_{C-O} , d_{C-O} , d_{M-C} , and ΔG_{Ads} . In short, these data suggest that the site dependence can contribute additional complexity in interpreting attractive and repulsive interactions at the M-CO interface, and that these interactions are delocalized in that they involve interactions directly at the adsorption site in addition to interactions with nearest neighbor atoms.

Supporting Tables and Figures

Table 1: Relative Atomic Fractions Measured by XPS. Note the relatively large Au intensity is due to the XPS measurements having a penetration depth beyond a monolayer.

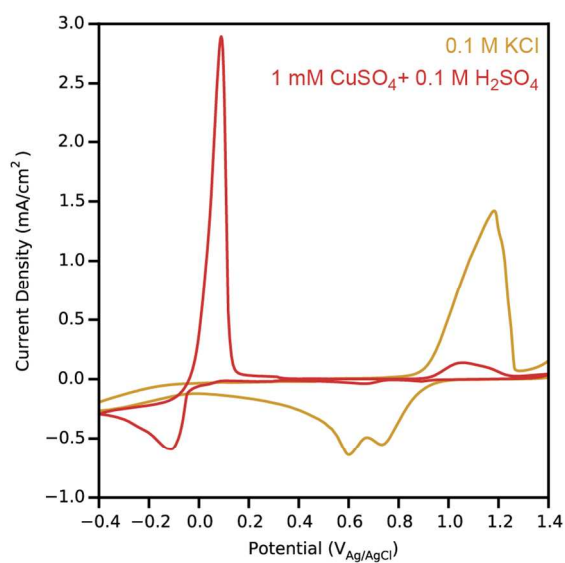
Sample	Au 4f (Relative Intensity)	Cu 2p3 (Relative Intensity)
Au/Cu $\Theta \sim 1/3$	89.7	10.2
Au/Cu $\Theta \sim 2/3$	87.6	12.3
Au/Cu $\Theta \sim 3/3$	80.0	19.9

Table 2: Calculated Thermodynamic Quantities for Cu-Enriched (111) Surfaces

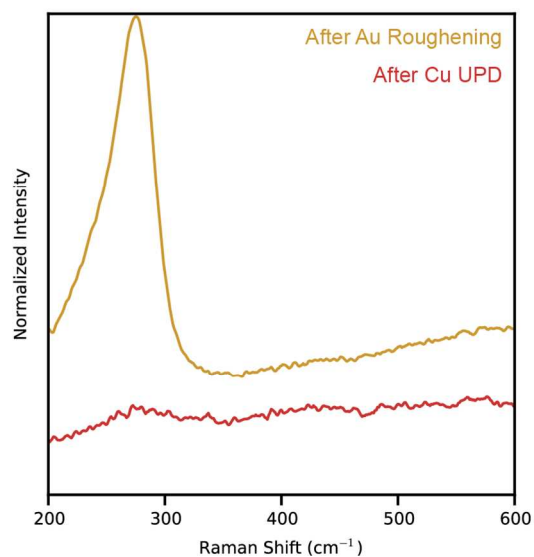
Geometry	$E_{\text{Electronic}}$	ZPE	$\int C_v dT$	-T(S)	G
CO (g)	-14.78	0.13	0.09	0.67	-15.22
H ₂ (g)	-6.77	0.27	0.09	0.43	-6.94
Au (111)	-81.59				
*CO	-96.53	0.20	0.07	-0.13	-96.39
*H	-84.74	0.14	0.01	-0.01	-84.60
Au/Cu $\Theta = 1/3$	-82.24				
Au _{Ads} *CO	-97.37	0.20	0.07	-0.13	-97.24
Cu _{Ads} *CO	-97.65	0.22	0.06	-0.10	-97.48
*H	-85.52	0.13	0.01	-0.02	-85.393
Au/Cu $\Theta = 2/3$	-82.52				
Au _{Ads} *CO	-97.79	0.20	0.07	-0.15	-97.67
Cu _{Ads} *CO	-98.11	0.21	0.07	-0.12	-97.96
*H	-85.93	0.14	0.01	-0.01	-85.80
Au/Cu $\Theta = 1$	-82.23				
*CO	-97.91	0.21	0.06	-0.11	-97.75
*H	-85.84	0.16	0.01	-0.01	-85.69
Cu (111)	-92.20				
*CO	-107.61	0.20	0.07	-0.13	-107.47
*H	-95.70	0.18	0.004	-0.01	-95.52

Table 3: Calculated Thermodynamic Quantities for (110) and (100) Facets

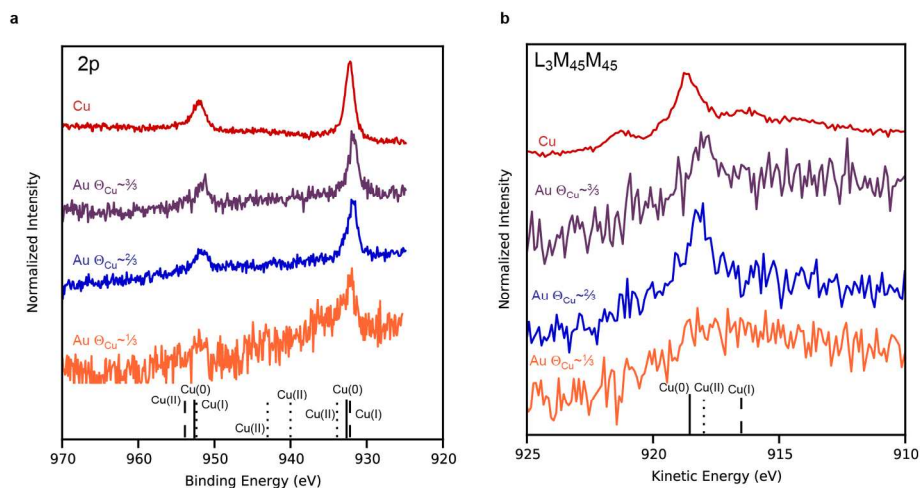
Geometry	E_{Electronic}	ZPE	∫ C_v dT	-T(S)	G
Au (110)	-74.66				
*CO	-90.03	0.19	0.08	-0.14	-89.91
*H	-78.13	0.17	0.01	-0.02	-77.97
Au (100)	-78.94				
*CO	-94.13	0.21	0.07	-0.11	-93.97
*H	-81.99	0.05	0.02	-0.05	-81.97
Au/Cu Θ=1 (110)	-77.99				
*CO	-93.72	0.21	0.07	-0.12	-93.57
*H	-81.48	0.16	0.04	-0.08	-81.36
Au/Cu Θ=1 (100)	-80.70				
*CO	-96.52	0.19	0.06	-0.10	-96.38
*H	-83.94	0.05	0.02	-0.05	-83.92
Cu (110)	-83.71				
*CO	-99.31	0.21	0.07	-0.12	-99.15
*H	-87.23	0.16	0.01	-0.01	-87.07
Cu (100)	-89.20				
*CO	-104.53	0.20	0.07	-0.14	-104.67
*H	-92.75	0.11	0.02	-0.02	-92.65



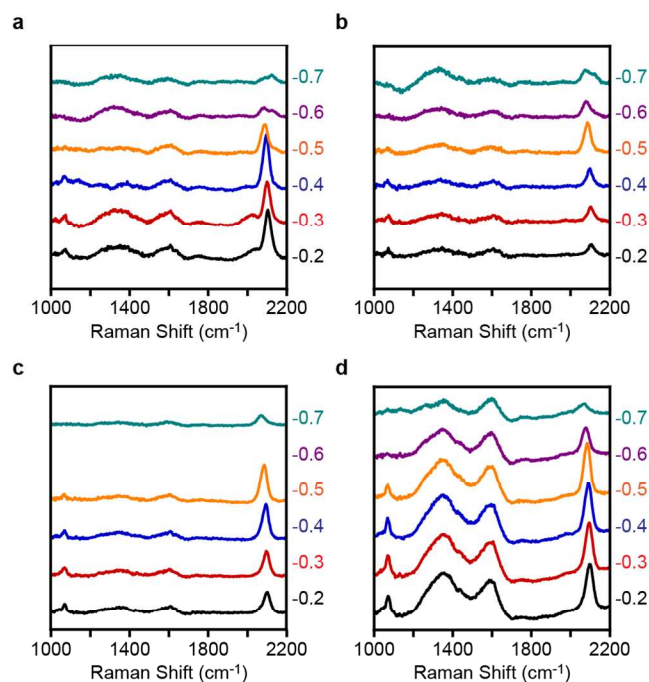
Supporting Figure 1. Typical cyclic voltammograms of roughened gold foil in 0.1 M KCl (yellow) and in 1 mM CuSO₄ + 0.1 M H₂SO₄ (red). The UPD window exists positive of ~0.0 V vs. Ag/AgCl, where bulk Cu deposition begins.



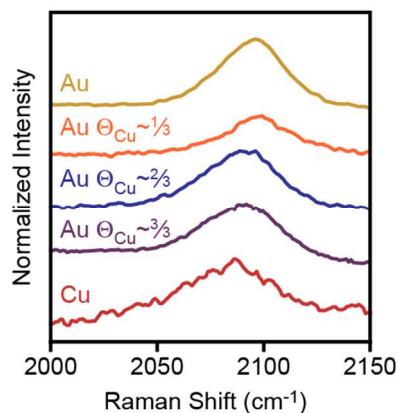
Supporting Figure 2. SER spectra before (yellow) and after (red) underpotential deposition of Cu monolayer onto roughened Au substrate. The peak at ~270 cm⁻¹ is associated with the vibration of adsorbed chloride ($\nu_{\text{Au-Cl}}$) on the surface.²³



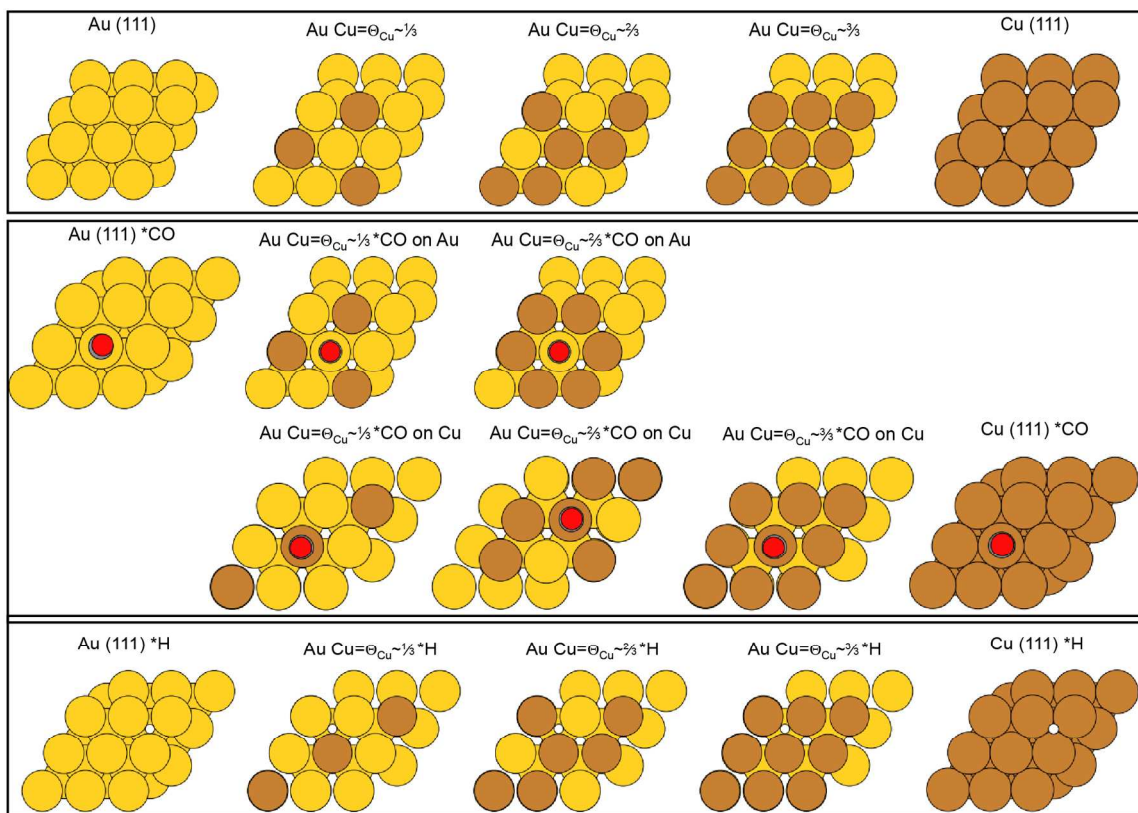
Supporting Figure 3. XPS and Auger Spectroscopy Characterization of the UPD Cu Oxidation State. (a) XPS of the Cu 2p region is indicative of Cu⁰ or Cu¹⁺. (b) Auger electron spectroscopy of the Cu L₃M₄₅M₄₅ region is indicative of Cu⁰ or Cu²⁺.²⁴ Together, these data suggest the presence of Cu in a primarily metallic (Cu⁰) state. An electropolished Cu foil (top, red) is shown as a comparison.



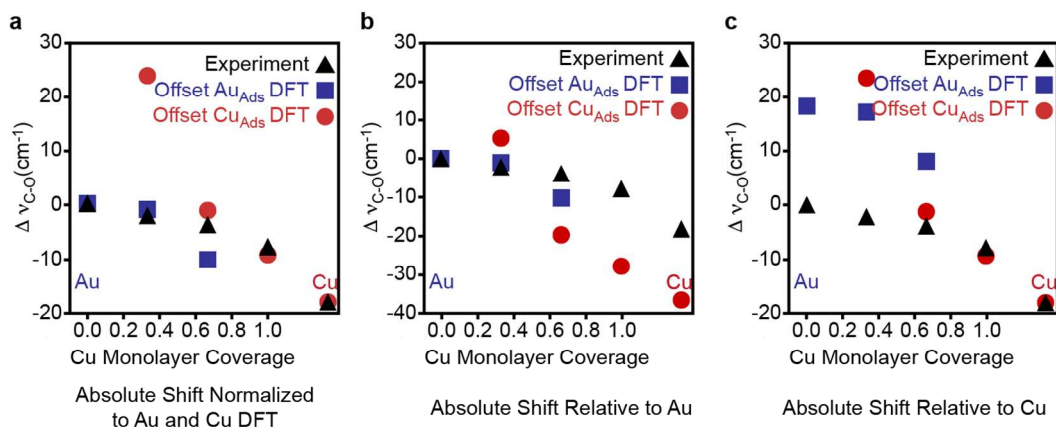
Supporting Figure 4. Typical potential dependent SER spectra during CO electrosynthesis. Potential dependent SER waterfall plots for Au (a), UPD Cu $\Theta=1/3$ (b), UPD Cu $\Theta=2/3$ (c), and UPD Cu $\Theta=3/3$ (d) The corresponding Stark slopes are 46 (a), 60(b), 60(c), and 57(d) cm⁻¹/V.



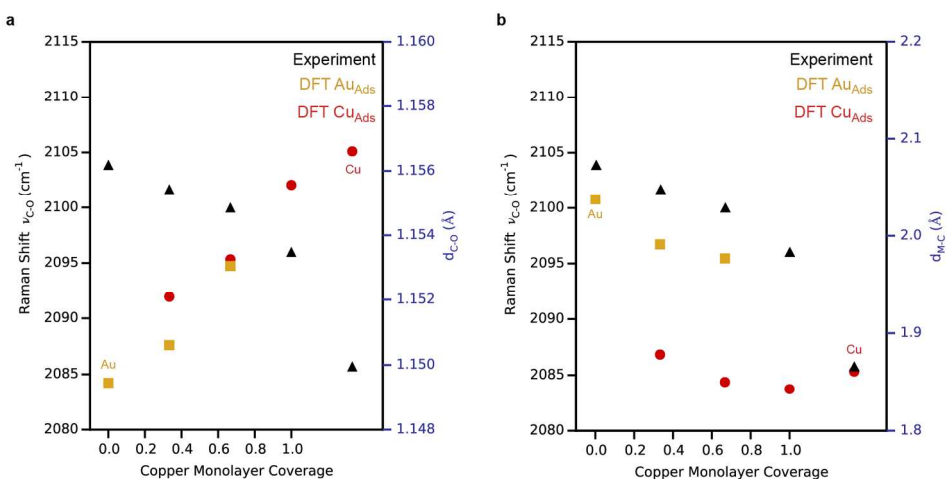
Supporting Figure 5. *In situ* SER spectra for different amounts of Cu-enrichment at -0.5 V vs. RHE.



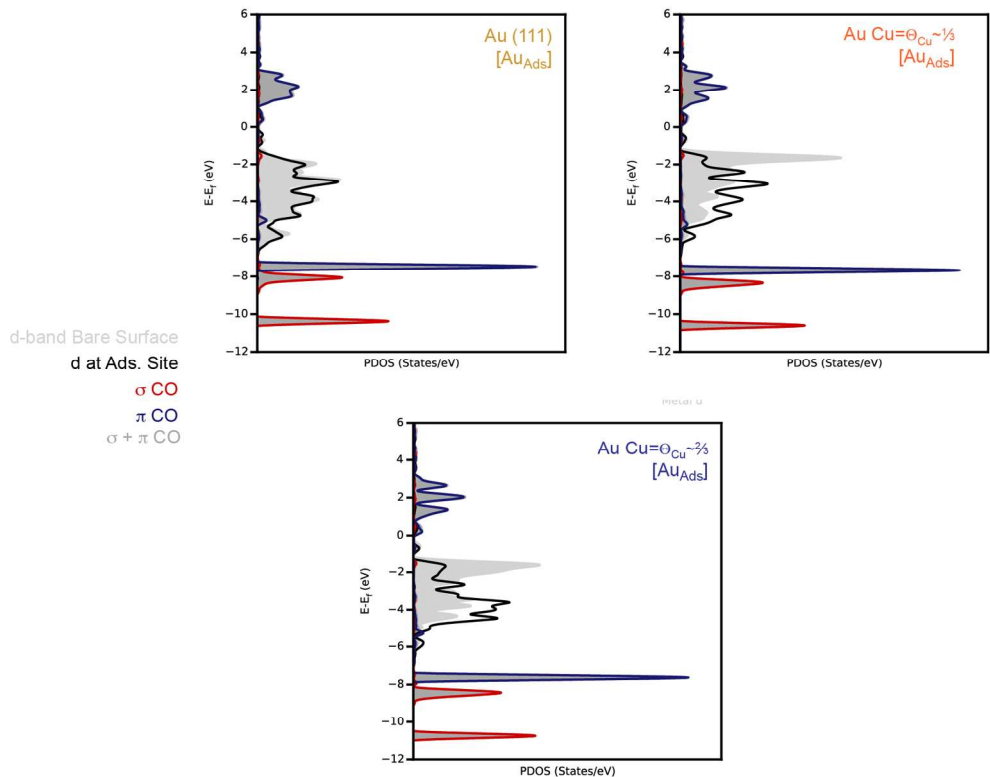
Supporting Figure 6. Optimized geometries Site Dependent DFT Calculations with Varying Extents of Cu Enrichment. Renders of the optimized bare (111) slabs (top), optimized slabs with CO adsorbed in the ontop position (middle), and optimized slabs with H adsorbed in the fcc hollow position (bottom).



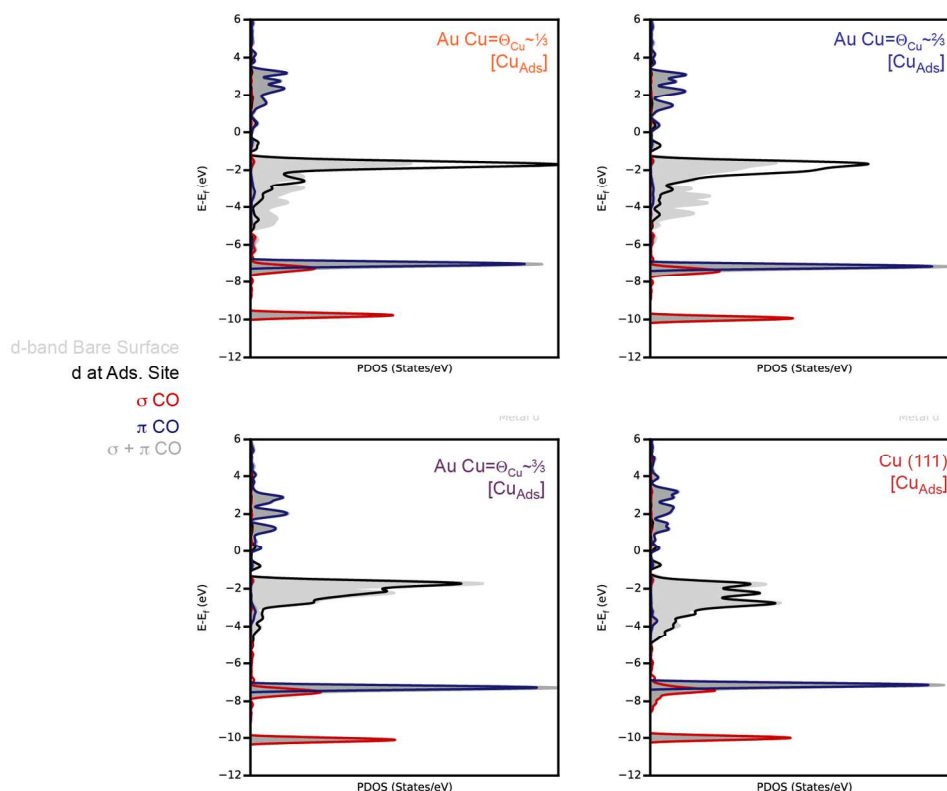
Supporting Figure 7. Comparison between experimentally measured C-O Raman shift and the calculated C-O vibrational frequencies. (a) The absolute Raman shift (experiment, black triangles) and calculated vibrational frequency shift (Au_{Ads} , blue squares and Cu_{Ads} , red circles) with the Au_{Ads} DFT points normalized to the Au experimental point and the Cu_{Ads} DFT points normalized to the Cu experimental point. (b) The absolute Raman shift (experiment, black triangles) and calculated vibrational frequency shift (Au_{Ads} , blue squares and Cu_{Ads} , red circles) with the Au experimental point set as zero. (c) The absolute Raman shift (experiment, black triangles) and calculated vibrational frequency shift (Au_{Ads} , blue squares and Cu_{Ads} , red circles) with the Cu experimental point (and corresponding Cu (111) DFT point) set as zero.



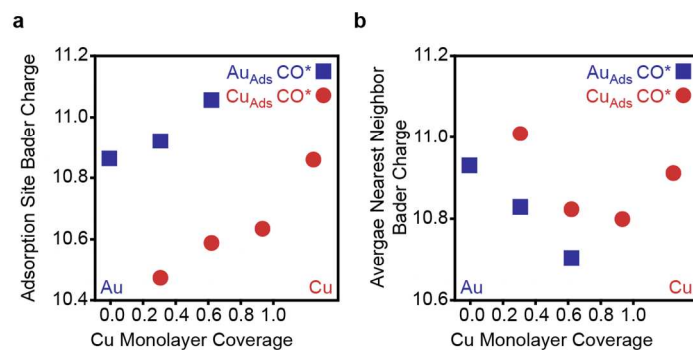
Supporting Figure 8. Comparison between experimentally measured Raman shift and the calculated characteristic C-O and C-M bond lengths. (a) A comparison between the measured Raman shift of $\nu_{\text{C-O}}$ (black triangles) and the DFT calculated C-O bond lengths ($d_{\text{C-O}}$) at Cu sites (red circles) and Au sites (yellow squares). (b) A comparison between the measured Raman shift of $\nu_{\text{C-O}}$ (black triangles) and the DFT calculated C-M bond lengths ($d_{\text{C-M}}$) at Cu sites (red circles) and Au sites (yellow squares).



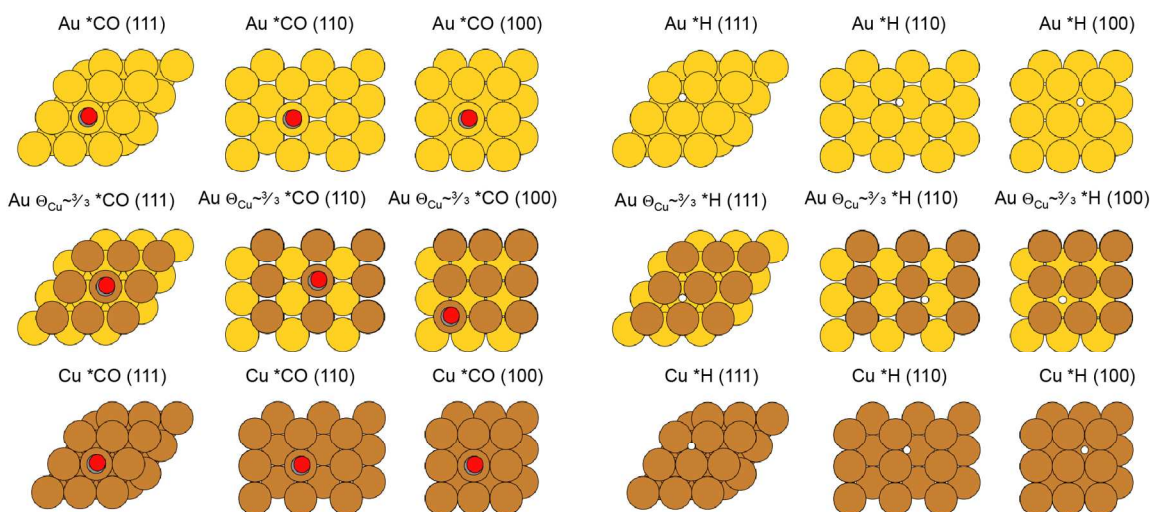
Supporting Figure 9. Projected density of states for Au adsorbed CO slab geometries. PDOS plots (clockwise from top left) for CO adsorbed at Au sites for Au (111), Au(111)-Cu $\Theta=1/3$, and Au(111)-Cu $\Theta=2/3$. The bare slab d-band (shaded, light grey), the d-band at the adsorption site atom (line, black), the σ CO orbitals (line, red), the π CO orbitals (line, blue), and $\sigma+\pi$ CO orbitals (shaded, dark grey) are all included.



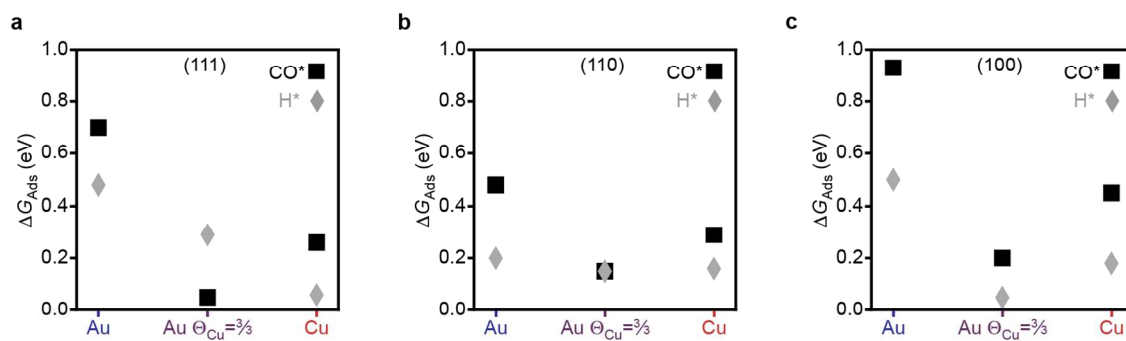
Supporting Figure 10. Projected density of states for Cu adsorbed CO slab geometries. PDOS plots (clockwise from top left) for CO adsorbed at Cu sites for Cu (111), Au(111)-Cu $\Theta=1/3$, Au(111)-Cu $\Theta=2/3$, and Au(111)-Cu $\Theta=3/3$. The bare slab d-band (shaded, light grey), the d-band at the adsorption site atom (line, black), the σ CO orbitals (line, red), the π CO orbitals (line, blue), and $\sigma+\pi$ CO orbitals (shaded, dark gray) are all included.



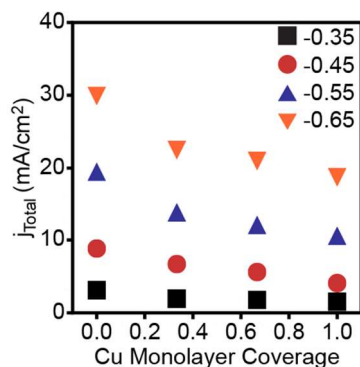
Supporting Figure 11. Bader partial charge density analysis at the CO adsorption site. (a) The Bader partial charge at the CO adsorption site (Au_{Ads} , blue squares and Cu_{Ads} , red circles). (b) The average Bader partial charge of the six nearest-neighbor atoms to the CO adsorption site (Au_{Ads} , blue squares and Cu_{Ads} , red circles).



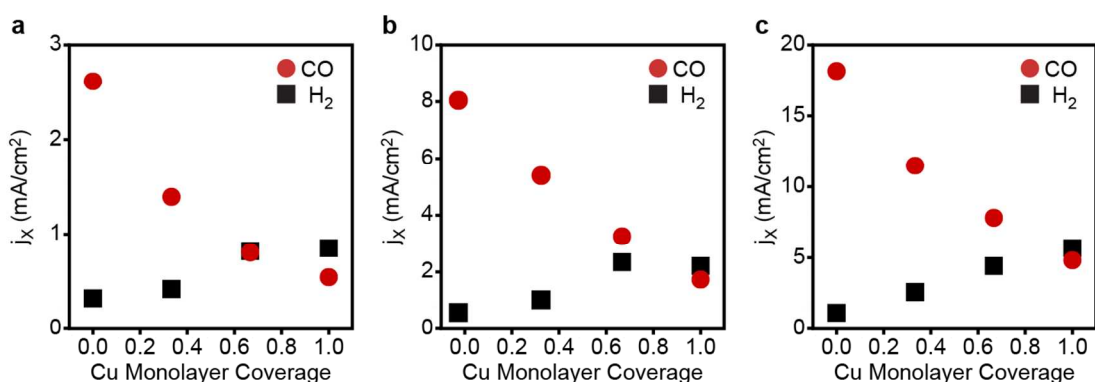
Supporting Figure 12. Optimized Geometries for Facet Dependence of H and CO Adsorption. Renders of the optimized geometries are depicted with the corresponding labels above the image



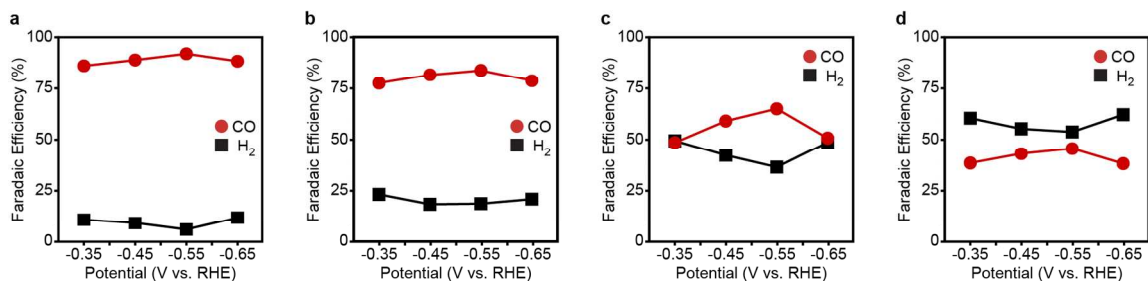
Supporting Figure 13. Facet Dependent Energetics of CO and H Adsorption
 Calculated adsorption energies for CO* (black squares) and for H* (gray diamonds) on the (111) (a), (110) (b), and (100) (c) facets.



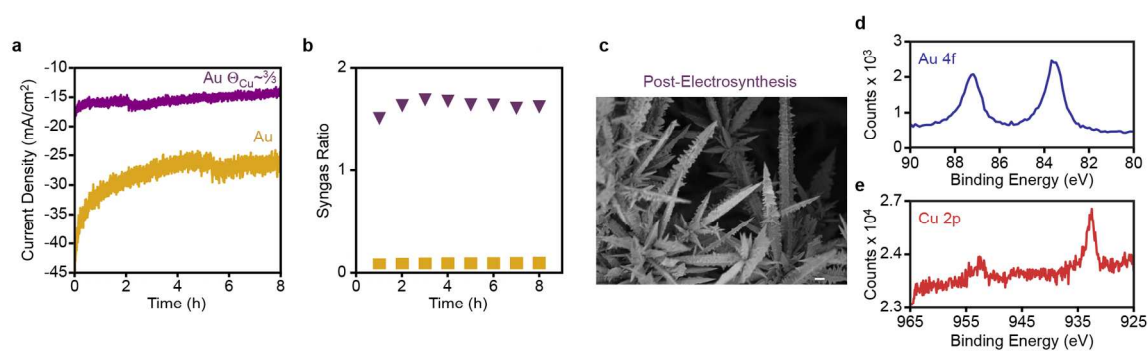
Supporting Figure 14. High total current densities are maintained for all Au needles enriched with Cu. Current density (mA/cm^2) as a function of Cu deposition at potentials of -0.35 (black squares), -0.45 (red circles), -0.55 (blue triangles), and -0.65 (orange inverted triangles) V vs. RHE.



Supporting Figure 15. Production of CO and H₂ varies as a function of Cu coverage extent. Partial current densities for CO (red circles) and H₂ (black squares) at potentials of -0.35 (a), -0.45 (b), and -0.55 (c) V vs. RHE.



Supporting Figure 16. Faradaic efficiencies as a function of potential for the (a) unmodified, (b) 1/3 Cu UPD modified, (c) 2/3 Cu UPD modified, and (d) 3/3 Cu UPD electrocatalysts.



Supporting Figure 17. Electrocatalyst stability over time. (a) Extended electrosynthesis for the bare Au and 3/3 Cu UPD modified electrocatalysts at -0.65 V vs. RHE. The initial drop in current density for the Au sample is due to visible delamination of mechanically unstable regions of the catalyst on the carbon paper (likely due to vigorous bubbling and stirring). (b) Syngas ratio over time. (c) Post-electrosynthesis SEM of the 3/3 Cu UPD modified electrocatalyst. XPS of the Au 4f (d) and Cu 2p (e) regions. Analysis of the XPS signal reveals 85.5 at% Au and 14.5 at% Cu signal ratio, which is similar to the values reported in Table 1.

References

1. Gao, P.; Patterson, M. L.; Tadayyoni, M. A.; Weaver, M. J. *Langmuir* **1985**, *1*, 173-176.
2. Perdew, J. P.; Burke, K.; Ernzerhof, M. *Phys. Rev. Lett.* **1996**, *77*, 3865-3868.
3. Kresse, G.; Furthmüller, J. *Phys. Rev. B* **1996**, *54*, 11169-11186.
4. Peterson, A. A.; Abild-Pedersen, F.; Studt, F.; Rossmeisl, J.; Nørskov, J. K. *Environ. Sci.* **2010**, *3*, 1311.
5. Liu, M.; Pang, Y.; Zhang, B.; De Luna, P.; Voznyy, O.; Xu, J.; Zheng, X.; Dinh, C. T.; Fan, F.; Cao, C.; de Arquer, F. P. G.; Safaei, T. S.; Mepham, A.; Klinkova, A.; Kumacheva, E.; Filleter, T.; Sinton, D.; Kelley, S. O.; Sargent, E. H. *Nature* **2016**, *537*, 382-386.
6. Blöchl, P. E. *Phys. Rev. B* **1994**, *50*, 17953-17979.
7. Kresse, G.; Joubert, D. *Phys. Rev. B* **1999**, *59*, 1758-1775.
8. Monkhorst, H. J.; Pack, J. D. *Phys. Rev. B* **1976**, *13*, 5188-5192.
9. Hansen, H. A.; Varley, J. B.; Peterson, A. A.; Nørskov, J. K. *J. Phys. Chem. Lett.* **2013**, *4*, 388-392.
10. Head, J. D.; Zerner, M. C., A. *Chem. Phys. Lett.* **1985**, *122*, 264-270.
11. Bahn, S. R.; Jacobsen, K. W. *Comput. Sci. Eng.* **2002**, *4*, 56-66.
12. Tang, W.; Sanville, E.; Henkelman, G. *J. Phys. Condens. Matter* **2009**, *21*, 084204.
13. Kudelski, A.; Pettinger, B. *Chem. Phys. Lett.* **2004**, *383*, 76-79.
14. Dunwell, M.; Lu, Q.; Heyes, J.; Rosen, J.; Chen, J. G.; Yan, Y.; Xu, B. *J. Am. Chem. Soc.* **2017**, *139*, 3774-3783.
15. Gajdo, M.; Eichler, A.; Hafner, J. *J. Phys. Condens. Matter* **2004**, *16*, 1141-1164.
16. Sung, S. S.; Hoffmann, R. *J. Am. Chem. Soc.* **1985**, *107*, 578-584.
17. Hammer, B.; Nørskov, J. K. *Nature* **1995**, *376*, 238-240.
18. Blyholder, G. *J. Phys. Chem.* **1964**, *68*, 2772-2777.
19. Dabo, I.; Wieckowski, A.; Marzari, N. *J. Am. Chem. Soc.* **2007**, *129*, 11045-11052.
20. Koper, M. T. M.; van Santen, R. A.; Wasileski, S. A.; Weaver, M. J. *J. Chem. Phys.* **2000**, *113*, 4392-4407.
21. Wasileski, S. A.; Koper, M. T. M.; Weaver, M. J. *J. Am. Chem. Soc.* **2002**, *124*, 2796-2805.
22. Shubina, T. E.; Koper, M. T. M. *Electrochim. Acta* **2002**, *47*, 3621-3628.
23. Leung, L. W. H.; Gosztola, D.; Weaver, M. J. *Langmuir* **1987**, *3*, 45-52.
24. Zhang, L.; Han, L.; Zhao, G.; Chai, R.; Zhang, Q.; Liu, Y.; Lu, Y. *Chem. Commun.* **2015**, *51*, 10547-10550.